Materials Advances

ROYAL SOCIETY OF CHEMISTRY

PAPER

View Article Online
View Journal | View Issue

Cite this: *Mater. Adv.*, 2020, 1, 794

Scalable solid-state synthesis of MoS_2–NiS_2/graphene nanohybrids as bifunctional electrocatalysts for enhanced overall water splitting†

Sunil P. Lonkar,* Vishnu V. Pillai and Saeed M. Alhassan *

In a confined nanoarchitecture, the transition metal sulphides (TMDs) exhibit a synergistic contribution towards exceptional electrocatalytic performance. Herein, we proposed an environment-friendly, *in situ* synthesis approach for MoS_2 wrapped NiS_2 nanohybrids uniformly dispersed on conductive graphene sheets. This solventless and technologically scalable process involves solid-state mixing of molybdenum and nickel salts and surfeit yet non-toxic elemental sulphur using ball-milling followed by thermal annealing. The resulting nanohybrids are composed of defect rich, heterostructured MoS_2–NiS_2 uniformly distributed within the surface of graphene and were used as a bifunctional electrocatalyst for overall water splitting. This synergistic hybridization of MoS_2–NiS_2/graphene has promoted a highly expanded surface, abundant electroactive centers, and a tailored conductive network, leading to enhanced water splitting efficacy. The nanohybrid exhibited superior catalytic performance for the HER with exceptionally low overpotentials in acidic (152 mV) and alkaline (141 mV) media, at a current density of 10 mA cm^{-2}. Likewise, a small OER overpotential of 320 mV was achieved under an alkaline medium. The resulting nanohybrid also evolved as a competent bifunctional electrocatalyst for optimal overall water splitting with a final cell voltage of 1.58 V with superior activity and stability. Therefore, the presented cost-effective and environment-friendly strategy provides high potential in the rational design and large-scale production of other nonprecious nanostructured bi-metallic sulphide materials for various energy and environmental applications.

Received 10th April 2020,
Accepted 28th May 2020

DOI: 10.1039/d0ma00192a

rsc.li/materials-advances

Introduction

Being confronted with ever-growing environmental problems, the explorations of clean and renewable energy sources that could contribute to sustainable energy production, conversion, and storage are urgently required.[1,2] In this context, electrochemical water splitting is the most promising, convenient, and green route to harvest hydrogen and oxygen for renewable energy and holds bright future prospects.[3,4] Nevertheless, due to the unavoidable dynamic overpotentials during the splitting of water molecules to generate hydrogen (HER) and oxygen (OER), the electrolysis efficiency is rigorously obstructed.[5] In this respect, the design and development of economical yet advanced electrocatalysts having lower overpotential of the HER and OER hold high promise and potential for further improvements in the efficiency of overall water splitting. Currently, noble metal-based commercial electrocatalysts (Pt hybrids/alloys for HER and Ir/Ru oxides/alloys for OER) exhibit extraordinary electrocatalytic properties (low overpotentials and longer stability) and are commonly considered as the benchmark electrocatalysts.[6,7] However, the utilization of these noble-metal catalysts in the large-scale water splitting technologies is severely impeded due to their scarcity and exorbitant cost. Hence, the quest for earth-abundant, stable, and economical electrocatalysts having high activity towards the HER and OER is still on.[8] In recent years, numerous novice combinations of the materials, including nonprecious-metals such as transition metal sulphides/oxides, chalcogenides, and mixed metal oxides, have been pursued as efficient electrocatalysts and have attracted significant attention.[9,10,11–13]

Among them, transition metal sulphides such as layered MS_2 (M = M, W) and non-layered M_xS_y (M = Ni, Co, Cu, Zn, *etc.*)

Department of Chemical Engineering, Khalifa University, P.O. box 127788, Abu Dhabi, 127788, United Arab Emirates. E-mail: saeed.alkhazraji@ku.ac.ae, sunil.lonkar@ku.ac.ae; Fax: +971-26075200; Tel: +971-26075944

† Electronic supplementary information (ESI) available: Materials and electrochemical characterizations, synthesis procedure of graphite oxide (GO); schematic illustration of possible reactions during MoS_2/NiS_2–G nanohybrid formation; TG-MS spectra of the precursor mix before thermal treatment; XRD pattern of the GO and TRG; SEM images of pristine MoS_2–NiS_2 nanohybrids; HRTEM images, FFT and SAED pattern of the MoS_2–NiS_2/G nanohybrid; TGA curves of MoS_2–NiS_2/G and graphene; XPS spectra of NiS_2 and GO; N_2 adsorption–desorption isotherm of pristine MoS_2–NiS_2; possible HER and OER mechanisms; calculations of active sites; tables of HER and OER activity comparisons; electrochemical analysis such as CV, EIS and CP stability tests for pristine MoS_2–NiS_2. See DOI: 10.1039/d0ma00192a

are at the forefront due to their unique structure, hydrogen binding activity, and excellent electrochemical performance.[14–20] However, most of the electrocatalysts exhibit stellar catalytic performance in a specific electrolyte media such as acidic, neutral, or alkaline and exhibit dwindling electrocatalytic efficiency under common electrolyte media. Similarly, their poor stability and inadequate electroactive sites have significantly hindered their electrocatalytic efficiency towards overall water splitting.[21,22] For example, molybdenum sulphide (MoS_2) based materials which hold a layered 2D structure have successfully demonstrated appropriate HER activity in acidic or neutral media.[23] However, the electrocatalytic performance of MoS_2 hybrids in alkaline electrolytes is significantly deprived, thus impeding the prospects of these materials toward overall water splitting.[24] On the other hand, nickel sulphide (Ni_xS_y) based electrocatalysts displayed excellent performance but only limited to alkaline media.[25,26] Hence, to overcome these impediments, bifunctional electrocatalysts for simultaneous HER and OER reactions were developed by coupling the non-noble transition metal sulphides/oxides, phosphides, nitrides, hydroxides, *etc.*[12,27] The improved performance for such bimetallic nanohybrids was primarily credited to their ample yet reactive redox sites, synergistic interfaces, and tailored conductivity.[28,29] Recently, a few specific Mo and Ni sulphide-based bimetallic nanohybrids such as Ni–MoS_2,[10] NiS/MoS_2,[30] MoS_2/Ni_2S_3,[31] MoS_2/Ni_3S_2,[32] MoS_2/NiS_2,[33] *etc.* have shown great promise as effective and inexpensive electrocatalysts for overall water splitting, predominantly owing to their fine-tuned synergistic activity and effective interface engineering. Nonetheless, the lack of inherent conductivity has emerged as a major demerit and obstructed these bifunctional nanohybrids from being the perfect substitute for noble-metal based electrocatalysts.[34] Hence, in order to increase the catalytic activities of these nanohybrids, hybridization with carbon substrates such as graphene, CNTs, *etc.* was much sought, and a few literature reports demonstrate such nanostructure-conductive support hybrids as an effective measure to enhance the overall water splitting efficiency of the electrocatalyst.[35,36] Furthermore, *in situ* growth of nanohybrids supported on conductive substrates can considerably minimize the particle aggregation, and eventually expose more catalytically active sites. Recently, Lin *et al.* reported defect rich MoS_2/NiS_2 nanohybrids supported on carbon cloth under a hydrothermal process followed by sulfudization for efficient overall water splitting.[37] Kuang *et al.* fabricated MoS_2/NiS_2 nanohybrids supported on 3D graphene foam as highly active electrocatalysts using hydrothermal treatment followed by a CVD method for efficient water splitting and suggested that the hetero-interfaces in the MoS_2–NiS_2 nanohybrid expedite the dissociation of H_2O molecules.[38] Similarly, the fabrication of Ni_9S_8 nanorod/O–MoS_2 supported on carbon cloth was also reported.[39] Zang *et al.* reported the fabrication of NiS_2@MoS_2 nanospheres anchored on a RGO surface using PVP as a surfactant.[19] These studies further highlighted the role of the substrate in controlling the aggregation of the resulting bi-metallic nano-sulphides and offer a high surface area that can boost the electrolyte contact. The overall outcome underlines the significance of designing defect-rich nanostructure systems directly supported on conductive substrates. The creation of such heterogeneous interfaces could provide abundant electroactive sites with enhanced surface area required for efficient overall water splitting. Although such methods lead to successful fabrication of hybrid electrocatalysts with exceptional electroactive properties, most of these methodologies employ intricate and multi-step hydro/solvothermal procedures and toxic surfactants, which could be potentially expensive and tedious for large scale implementations. Similarly, methods that involve direct growth on the Ni foam substrate can jeopardize the electrocatalyst compositions and loadings, and also poor stability in an acidic environment can potentially limit Ni foam supported catalysts for wide-scale applications. Hence, facile and scalable preparation of such heterostructured bifunctional nanohybrid electrocatalysts is the key for real-time large-scale sustainable energy production through overall water splitting.

Herein, we put forward a simplistic *in situ* strategy to fabricate heterostructured MoS_2–NiS_2 hybridized with graphene as a bifunctional electrocatalyst for overall water splitting. In this environmentally benign solid-state process, the non-noble Mo:Ni metal precursors, elemental sulphur (a surplus petroleum industry by-product), and graphite oxide (GO) were ball milled to ensure robust precursor mixing and sufficient metal–sulphur intercalation within the GO substrate. The resulting mixture was thermally annealed under controlled conditions. Under thermal treatment, the sulfudization of the metal precursors into bi-metallic sulphides and simultaneous thermal reduction of GO into graphene was achieved. The graphene substrate ensured the uniform distribution of bi-metallic sulphides with an optimal concentration of the catalytically reactive sites and high surface area. As a result, remarkable overall water splitting was achieved at relatively low onset potential and higher current densities with exceptional electrochemical stability. The resulting bi-functional MoS_2–NiS_2/graphene electrocatalyst exhibited competitive efficiencies compared to the state-of-the-art electrocatalytic materials used for water splitting. Also, the reported solid-state process holds high potential for facile and large-scale production of other nanostructured bi-metallic sulphide-based electrocatalysts for sustainable energy production.

Experimental

Preparation of MoS_2–NiS_2/graphene nanohybrids (MoS_2–NiS_2/G)

In a typical procedure, a stoichiometric quantity of the metal precursors, namely ammonium tetrathiomolybdate (NH_4MoS_4) and nickel oxalate (C_2NiO_4), graphite oxide, and elemental sulphur was continuously homogenized under ball milling (IKA ULTRA-TURRAX®-Germany). This special tube-drive controlled homogenizer was run at 4000 rpm for 60 min, and mixing was facilitated using stainless-steel balls (10 balls, each weighing 509.3 mg). The ball milling was expected to uniformly distribute and intercalate the metal precursors and sulphur particles within the layered graphite oxide. Subsequently, the

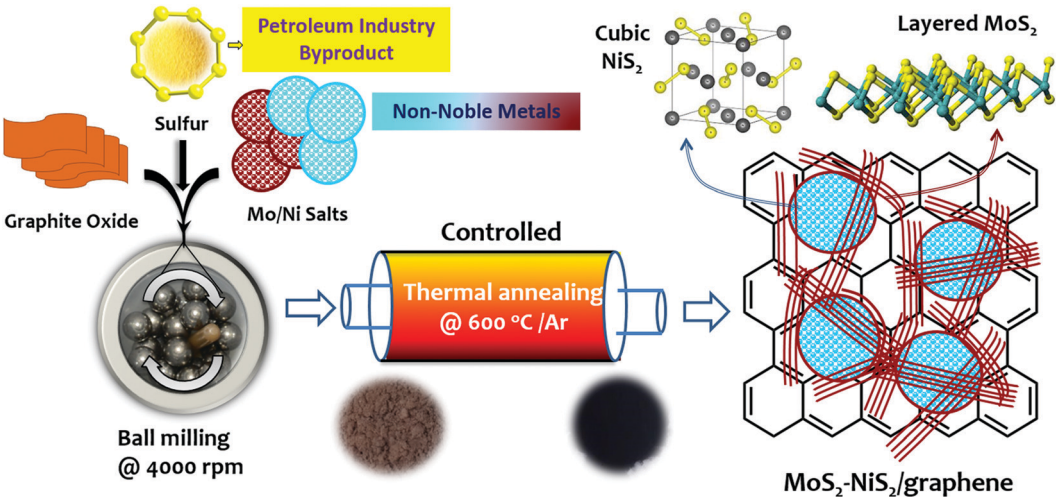

Scheme 1 Schematic representation of the preparation of the MoS_2–NiS_2/G nanohybrid.

pre-mixed precursor mixture was subjected to thermal treatment inside a tube furnace at 600 °C for 2 hours with persistent heating (5 °C min^{-1}) under incessant inert gas flow (argon) to finally achieve the MoS_2–NiS_2/graphene nanostructured hybrid (Scheme 1). An apparent colour transformation was also noticed from brownish (pre-mix) to greyish-black (post-annealing). For comparison, a similar procedure was applied to prepare pristine MoS_2–NiS_2 nanohybrid, MoS_2, and NiS_2 nanoparticles without GO.

Results and discussion

Electrocatalyst synthesis and characterization

Scheme 1 represents the realization of MoS_2–NiS_2/G nanohybrids prepared *via* solid-state synthesis. In this facile preparation, the Mo:Ni precursors, elemental sulphur and GO were first homogenized under high-speed milling. The uniform homogenization was expected to provide support for consistently formed mixed-metal nucleation sites. Then, under controlled thermal treatment, Mo and Ni ions liberated through thermal decomposition are concurrently reacted with *in situ* produced reactive gaseous sulphur species to form heterostructured MoS_2–NiS_2 nanoparticles within the thermally reduced graphite oxide layers. Similarly, under thermal treatment, the GO undergoes a thermal reduction to form graphene, which could provide ample surface support for resulting in uniform dispersion of nanosized heterostructured MoS_2–NiS_2 in the resulting nanohybrid. The formation of MoS_2–NiS_2/G was further confirmed by the colour change from brownish (precursor mix) to greyish-black (final nanohybrid). Moreover, the TGA-MS spectra (Fig. S1, ESI†) of the pre-thermally treated sample indicates that the formation of the MoS_2–NiS_2/G nanohybrid proceeds with the liberation of various gaseous species such as water vapour (m/z = 18), CO_2 (m/z = 44), and S ionic species (sulfidic sulphur, S_x^{2-}, m/z = 16), SO_2 (m/z = 64). These results suggest that the process is free from the formation of noxious hydrogen sulphide (m/z = 32). The possible reaction involved in the formation of this nanohybrid is presented as Scheme S1 (ESI†).

The crystalline structure and crystal phase composition of the as-obtained MoS_2–NiS_2/G nanostructured hybrids were investigated by using powdered X-ray diffraction (PXRD) analysis (Fig. 1a). Evidently, XRD diffractograms show sharp reflections of the MoS_2–NiS_2/G nanohybrid which clearly match with the characteristic JCPDS patterns for MoS_2 (JCPDS No. 17-0744)[40] and NiS_2 (JCPDS No. 65-3325)[41] showing peaks at 14.38, 33.11, 38.95, 49.64, and 58.72° corresponding to the (002), (101) and (110) planes of MoS_2 and peaks at 27.19, 31.57, 35.38, 38.92, 45.17, 53.17, 56.16, 58.62, and 61.06° corresponding to the characteristic planes of NiS_2 namely, (111), (200), (210), (211), (220), (311), (222), (023) and (321), signifying the presence of a pyrite-type cubic structure of NiS_2.[42] Moreover, the disappearance of the distinctive GO peaks around $2\theta = 9.7°$ (Fig. S2, ESI†) and the emergence of a new broad peak around $2\theta = 26°$ was exclusively specified to the distinguishing (002) planes of graphene, and this change asserted the successful *in situ* thermal reduction of the graphite oxide into graphene.[43] Hence, the overall XRD result clearly confirms the successful *in situ* formation of highly crystalline phase pure MoS_2–NiS_2 *in situ* formed within a graphene framework.

The morphology of MoS_2/NiS_2 was investigated by SEM and TEM imaging studies. The SEM images shown in Fig. 1b1 reveal the *in situ* formation of numerous mixes of spherical and layered nano-assemblies of MoS_2–NiS_2, which are uniformly distributed within the graphene surface. Whereas for pristine MoS_2–NiS_2 (Fig. S3, ESI†), a significant particle agglomeration was observed. The elemental maps (Fig. 1b2) indicated a uniform dispersion of Mo, Ni, S, and C elements, which further confirmed the *in situ* formed and well exposed MoS_2–NiS_2 nanohybrids within the layered graphene. Similarly, the TEM images also indicated the nanoscale features of the MoS_2–NiS_2/G nanohybrids. The MoS_2 nanolayers are decorated around NiS_2 nanoparticles, and the resulting nanohybrid was uniformly supported on the few layered graphene surface (Fig. 1c1, c2 and Fig. S4, ESI†). Moreover, in addition to the uniform distribution,

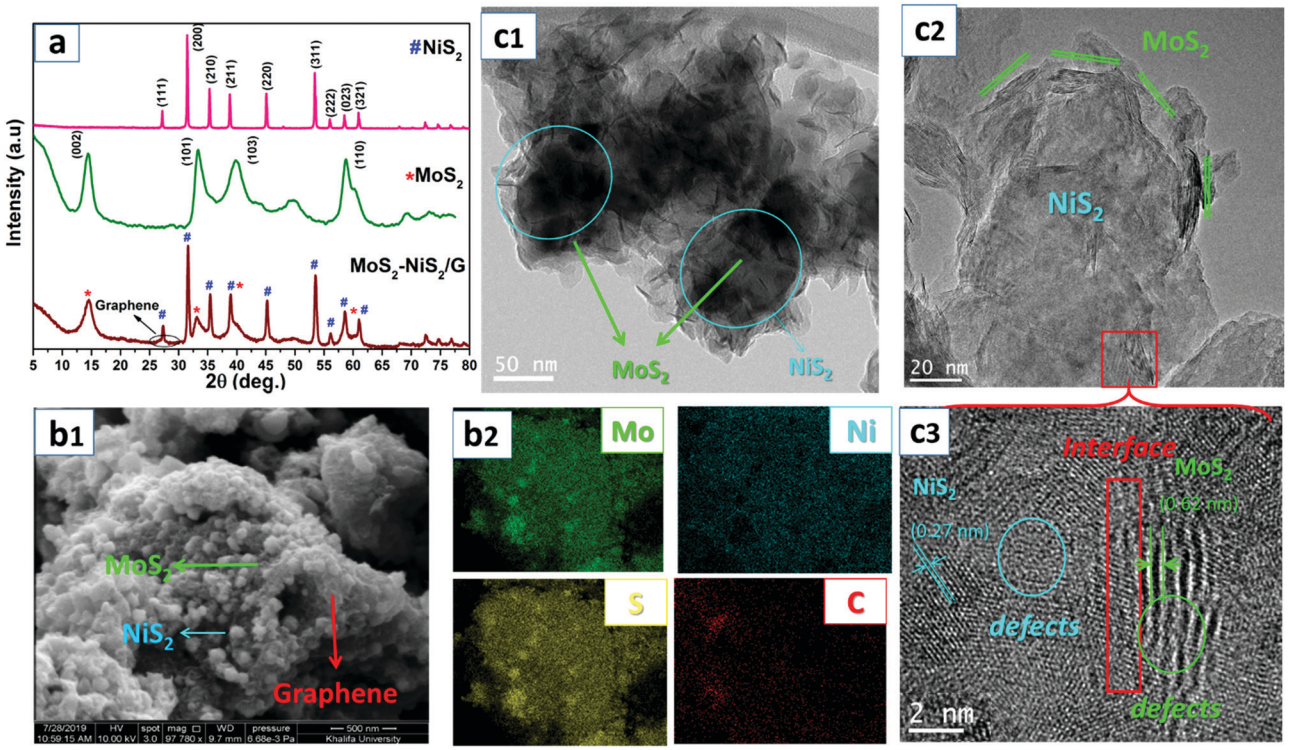

Fig. 1 X-ray diffraction pattern of NiS_2, MoS_2, and MoS_2–NiS_2/graphene nanohybrids (a), SEM and elemental mapping (b1 and b2), and TEM and HRTEM (c1–c3) of the MoS_2–NiS_2/G nanohybrids.

the strong adhesion between MoS_2 and NiS_2 nanoparticles with some discontinuous spots in the crystal fringes were also observed (Fig. S5, ESI†). Such intermittent spots can be accounted for by the defect formation in both the MoS_2 and NiS_2 lattice during the *in situ* synthesis process and can be advantageous for targeted electrocatalytic applications.[37] Furthermore, the high-resolution TEM image confirms the well-defined crystal structure and formation of the heterojunction interface (Fig. 1c3 and Fig. S5, ESI†), where the interplanar lattice distance of 0.64 and 0.28 nm can be correspondingly assigned to (002) and (210) crystal planes of MoS_2 and NiS_2.[38] As evidenced, the heterojunction formation amongst the two planes (002) of MoS_2 and (210) of NiS_2 was expected to function as the centre of water dissociation, wherein hydrogen is inclined to be adsorbed by MoS_2 and ^{-}OH will be intensely adsorbed by NiS_2.[44,45] Also, the presence of strong interfaces between MoS_2 and NiS_2 planes could facilitate the favourable electron transportation, leading to a promising synergistic effect. Furthermore, the distinct polycrystalline features observed in the Fourier transformation (FFT) and the selected area electron diffraction (SAED) pattern perfectly correlates with the MoS_2–NiS_2 affirming their cohabitation (Fig. S5, ESI†) and such synergism is advantageous for the intended electrocatalytic reactions. Similarly, the TGA of MoS_2–NiS_2/G in the air indicated the various phase changes (Fig. S6, ESI†). The weight loss around 400 °C was ascribed to the burning of graphene in the air, which was affirmed by the TGA curve of pristine graphene in the same temperature range. The weight loss after 600 °C was attributed to the oxidation of sulphides into oxides. Therefore, the as-prepared MoS_2–NiS_2/G nanohybrids can be determined to contain about 9.7 wt% graphene and around 90 wt% MoS_2–NiS_2.

The elemental compositions and the surface oxidation states of the elements present in the resulting MoS_2–NiS_2/G heterostructure were analysed by X-ray photoelectron spectroscopy (XPS). The XPS survey spectrum shown in Fig. 2(a) indicates the characteristic signals assigned for Mo 3d, Ni 2p, and S 2p from the MoS_2–NiS_2 heterostructure and C 1s and O 1s peaks assigned for graphene. The absence of any unknown peak confirms the purity of the as-obtained heterostructured MoS_2–NiS_2 phases in graphene. The high-resolution peaks of the Mo 3d 2(a1) deconvoluted into two prime peaks at centered at 228.9 and 232.5 eV, which are ascribed to the Mo $3d_{5/2}$ and Mo $3d_{3/2}$ modes, respectively and designate the presence of Mo in +4 oxidation state of the MoS_2.[46] The presence of Mo^{6+} peaks was expected to be caused by the air oxidation of the MoS_2 surface. Similarly, the deconvolution of the Ni 2p XPS spectra (Fig. 2a2) resulted in two core peaks appearing at 855.6 and 873.4 eV, accredited to the Ni $2p_{3/2}$ and Ni $2p_{1/2}$, respectively and present in +2 oxidation state. Also, both Ni $2p_{3/2}$ and Ni $2p_{1/2}$ give additional satellite peaks. The neighbouring S 2s peak at 227.5 eV represents the chemical state of sulphur species bonded with Mo and Ni ions. On the other hand, the deconvolution of the S 2p peak resulted in three peaks, Fig. 2(a3), namely at 162.91 (S $2p_{3/2}$) and 163.94 eV (S $2p_{1/2}$), implying the presence of unsaturated S atoms on the Ni–S and Mo–S sites of divalent sulphide ions (S^{2-}) in MoS_2. The peak positioned at 161.81 resembles the S $2p_{3/2}$ orbitals linked with Ni–S bonding.[47] The S 2p peak around

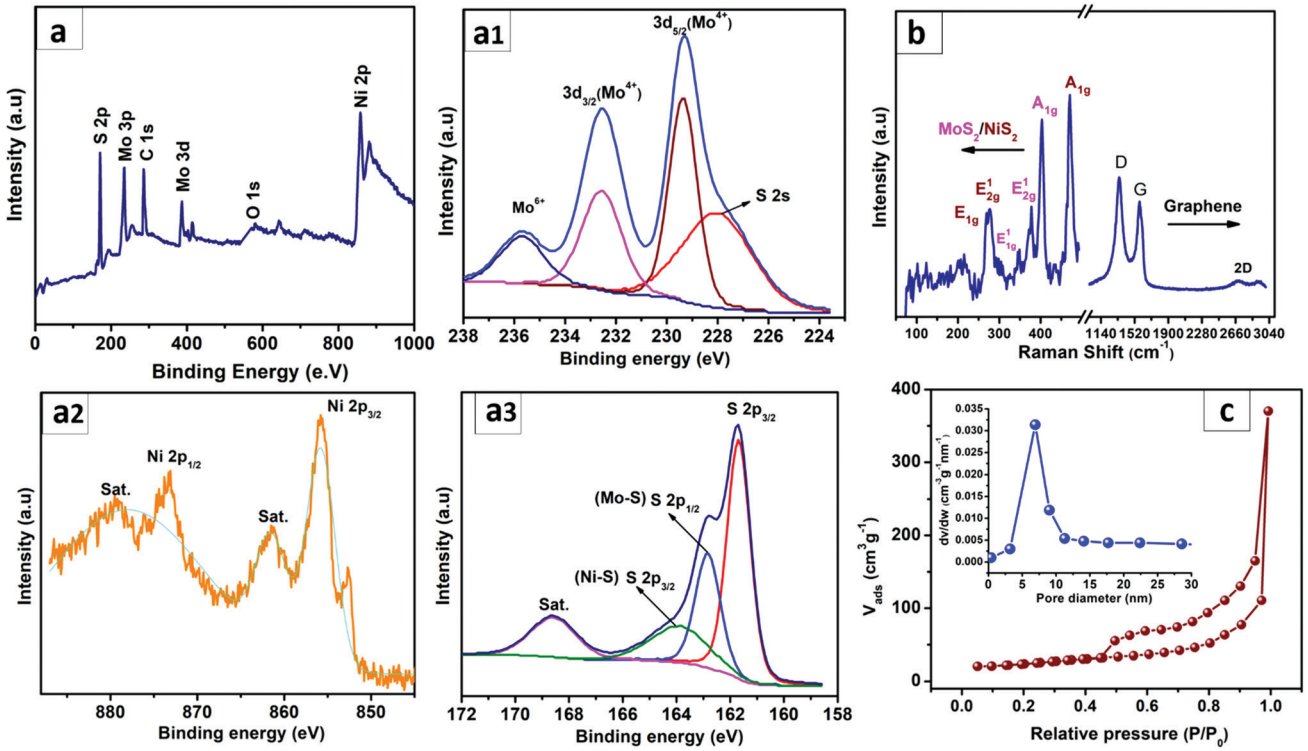

Fig. 2 XPS survey spectrum of the MoS_2–NiS_2/G nanohybrids (a), high resolution XPS spectrum of Mo 3d (a1), Ni 2p (a2) and S 2p (a3), and Raman spectrum (b) and N_2 adsorption–desorption isotherm (inset: pores size distribution) (c).

168.5 could be due to sulphate formation oxidation during XPS analysis.[48] A slight blue shift in the Ni 2p peaks in the MoS_2–NiS_2/G compared to the pristine NiS_2 (Fig. S7, ESI†), designates possible electronic interactions between MoS_2 and NiS_2 that are expected to promote the redistribution of the charges at their interfaces.[49] Similarly, compared to GO, the decrease in the O 1s peak and increment in C 1s for MoS_2–NiS_2/G (Fig. S7, ESI†) confirms the *in situ* reduction of GO into graphene. Raman spectroscopy was used to characterize the vibrational frequencies in the resulting MoS_2–NiS_2/G nanohybrid. Fig. 2b reveals the characteristic peaks of MoS_2 at 375 and 404 cm^{-1}, which correspond to the in-plane $E_{2g}{}^1$ and out-of-plane A_{1g} vibrational modes, respectively.[50] Similarly, peaks appeared at around 272, 280 and 475 cm^{-1} indicating the characteristic A_{1g} and E_g modes of NiS_2.[51] The hypsochromic shift of $E_{2g}{}^1$ and A_{1g} of MoS_2 in the nanohybrid compared to pristine MoS_2 further signifies the existence of electronic interactions between MoS_2 and NiS_2 in the heterostructured nanohybrids, which would soften the S–Mo bonds and thus decrease the vibration frequencies.[52] The Raman spectra of the nanohybrid (Fig. 2b) exhibited two distinct bands at 1341 and 1594 cm^{-1} conforming to the distinctive D and G bands with a small 2D band peak at 2710 cm^{-1} originating from the few-layer graphene framework of the hybrid.[53] Moreover, the intensity ratio of D band to G band for MoS_2–NiS_2/G (I_D/I_G = 1.19) was observed to be higher than that of pristine GO (I_D/I_G = 1.01), as displayed in Fig. S8 (ESI†). The improved I_D/I_G intensity ratio further indicates the reduction of GO into graphene. The surface features of the resulting nanohybrid were elucidated using the N_2 adsorption–desorption isotherm and shown in Fig. 2c. The measured Brunauer–Emmett–Teller (BET) specific surface area (105 $m^2\ g^{-1}$) and pore volume (1.05 cc g^{-1}) of the MoS_2–NiS_2/G nanohybrid were noted to be significantly higher than that of pristine MoS_2–NiS_2 (54.8 $m^2\ g^{-1}$ and 0.65 g^{-1}) as shown in Fig. S9 (ESI†). The presence of graphene was proven beneficial in improving the overall specific surface area of the resulting nanohybrids. Likewise, the corresponding pore size distribution plot calculated from adsorption isotherms indicates that the MoS_2–NiS_2/G nanohybrid exhibits a large number of mesopores mainly between 5 and 10 nm (inset of Fig. 2c). The increased specific surface area and the elevated porous structure is greatly beneficial for maximizing the number of catalytically active sites and efficient electron transfer.[54] Moreover, the adsorption–desorption isotherm of MoS_2–NiS_2/G can be categorized as a type IV isotherm, which further evidences that the obtained nanohybrid is a mesoporous MoS_2–NiS_2/G nanohybrid material.

Hydrogen evolution reaction (HER) study

The HER electrocatalytic performance of the resulting MoS_2–NiS_2/G nanohybrid was investigated using linear sweep voltammetry (LSV) at a scan rate of 5 mV s^{-1} between 0.5 and 0.1 V *vs.* RHE (reversible hydrogen electrode) in an Ar-saturated 0.5 M H_2SO_4 and 1 M KOH aqueous solution, respectively. For comparison, the MoS_2/NiS_2 nanohybrid, and pristine MoS_2 and NiS_2 nanoparticles were also assessed for their HER performance. Pure graphite sheets without any catalyst loading were also tested under identical conditions for the blank control. IR compensation was employed and the normalized

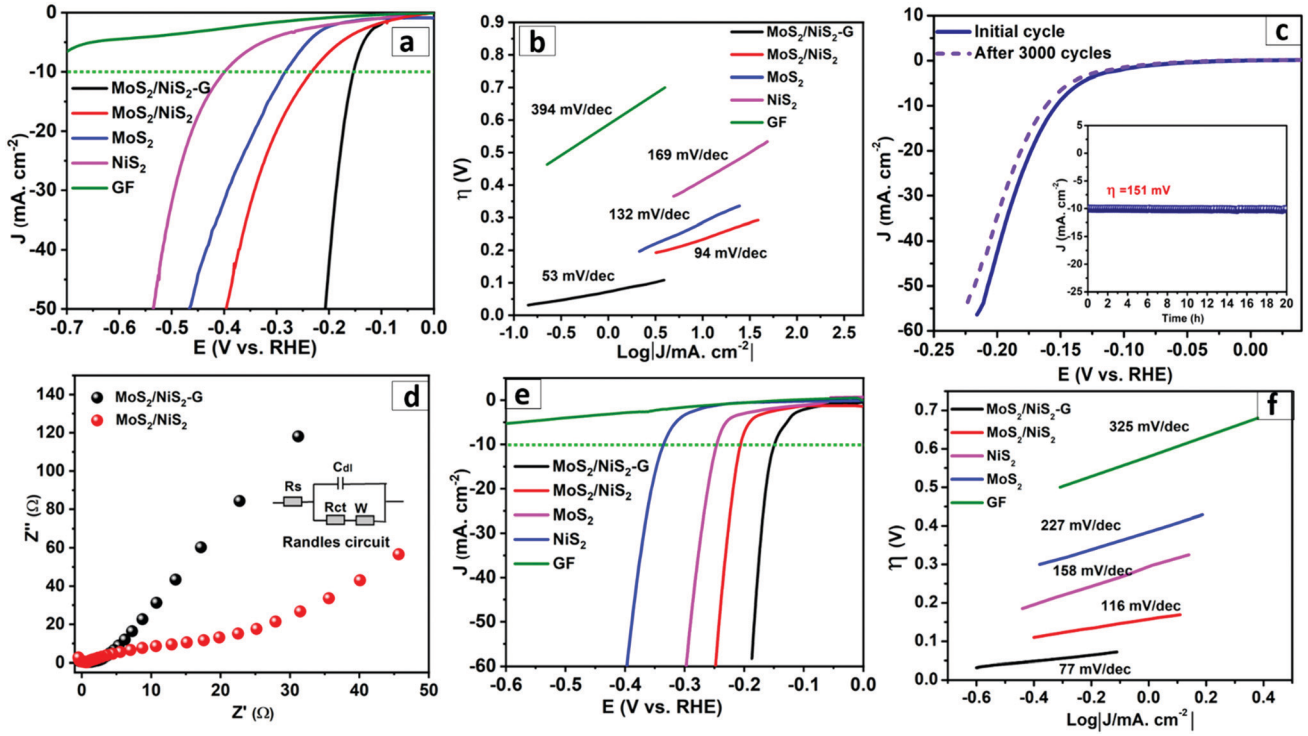

Fig. 3 (a) Polarization curves in 0.5 M H_2SO_4, (b) the corresponding Tafel plots of the obtained HER samples, (c) polarization curve before and after 3000 CV cycles (inset: chronopotentiometric curve of HER) for MoS_2–NiS_2/G, (d) EIS curves for MoS_2–NiS_2/G and MoS_2–NiS_2, (e) polarization curves in 1 M KOH and (f) the corresponding Tafel plots.

data were used for the analysis. Fig. 3a presents the corresponding polarization curves obtained by plotting the current density (J) *versus* the applied potential (V) in 0.5 M H_2SO_4. The MoS_2–NiS_2/G nanohybrid electrode showed onset potential at 90 mV and a low overpotential (η_{10}) of 152 mV to reach cathodic 'J' of 10 mA cm^{-2}. The nanostructured MoS_2–NiS_2 hybrids demonstrate the onset potential of 99 mV and an overpotential of 230 mV to reach cathodic 'J' of 10 mA cm^{-2} (η_{10}). Similarly, both pristine MoS_2 and NiS_2 display lower HER electrocatalytic activity, and the onset potentials were recorded to be 211 and 340 mV, respectively. The blank graphite was observed to have insignificant HER activity over the tested potential range. Similarly, the electrocatalytic mechanism involved in the HER was revealed by the Tafel plot (overpotential *vs.* log$j$). The Tafel slopes of the MoS_2–NiS_2/G nanohybrid, nanostructured MoS_2–NiS_2, MoS_2, and NiS_2 were calculated as 53, 94, 132, and 169 mV dec^{-1}, respectively (Fig. 3b). Generally, a smaller Tafel slope defines a faster rate of HER with smaller energy.[55] The much lower Tafel slope value of the MoS_2–NiS_2/G nanohybrids suggests the accelerated HER catalytic rate and implies the highly promising HER catalytic kinetics of MoS_2–NiS_2/G. The recorded Tafel slope (53 mV dec^{-1}) for MoS_2–NiS_2/G further underlines that the HER follows the Volmer–Heyrovsky mechanism (Scheme S2, ESI†).[56] Such remarkable HER catalytic activity of MoS_2–NiS_2/G was ascribed to the plentiful yet exposed active sites and defect-rich MoS_2–NiS_2 heterostructures uniformly distributed within the graphene conductive network, which exhibit unique synergy. Moreover, the *in situ* growth strategy was expected to increase the synergy between MoS_2–NiS_2 and the graphene substrate, leading to enhanced electronic coupling, which could expedite the better electron and ion transportation required to deliver enhanced HER performance. The recorded HER activity of the MoS_2–NiS_2/G nanohybrid was noted to outperform most of the previous studies based on non-noble metal heterostructured sulphides in acidic electrolyte (Table S1, ESI†). The stability and robustness are other important parameters that are associated with the performance of an electrocatalyst.[57] The long-term stability of the MoS_2–NiS_2/G nanohybrids was assessed by performing 3000 continuous CV cycles in 0.5 M H_2SO_4. Fig. 3c displays the assessment of the polarization curves of the hybrids after the 1st cycle and 3000th cycle, respectively. The results suggest a very marginal difference in the LSV curves and negligible loss of the catalytic performance highlighting the remarkable catalytic stability of the resulting MoS_2–NiS_2/G. Furthermore, the electrochemical durability of the MoS_2–NiS_2/G nanohybrids was tested by applying a constant current density of 10 mA cm^{-2}, and the results indicated that MoS_2–NiS_2/G delivered stable potential values for 20 h in 0.5 M H_2SO_4.

The EIS study further elucidates electron transfer at the catalyst interface. The EIS displays differential impedances for MoS_2–NiS_2/G and MoS_2–NiS_2 (Fig. 3d), where the former brings a lower charge-transfer resistance (R_{ct}) than pristine MoS_2–NiS_2. The small R_{ct} confirms the fast charge transfers at the interface, and thus better electro-catalytic performance was achieved for MoS_2–NiS_2/G, which is also supported by a shorter Warburg-type

line suggesting faster ion diffusion from outside of the electrolyte to the inside of the catalyst.[58] Furthermore, in order to estimate the effective active area (ECSA), the double-layer capacitance (EDLC) at the solid–liquid interface of the catalysts was measured from CV analysis. The capacitance (C_{dl}) was measured by plotting $\Delta j = j_a - j_c$ at an applied potential (0.25 V *vs.* RHE) *versus* the scan rate (Fig. S8, ESI†).[44] The calculated C_{dl} for MoS_2–NiS_2/G (6.5 mF cm^{-2}) is more significant than that of MoS_2–NiS_2 (1.2 mF cm^{-2}), and the higher C_{dl} value validates the more proficient mass and charge conveyance competence on MoS_2–NiS_2/G for efficient HER.[59]

Similarly, the calculated value of ECSA for the MoS_2–NiS_2/G was ~75 cm_{ECSA}^2, considerably greater in comparison to the pristine MoS_2–NiS_2 (~15 cm_{ECSA}^2, Fig. S10, ESI†). Such increment of ECSA is directly proportional to the abundance of active sites in the MoS_2–NiS_2/G, which was positively credited to the presence of graphene, which contributes to the improved electrocatalytic properties. Similarly, to get an insight into the active sites present on the resulting hybrids, voltammetric charge computation was employed. As derived from CV calculations (Fig. S11, ESI†), the MoS_2–NiS_2/G gives a value of 5.6×10^{-2} mol mg^{-1}, which is double the magnitude of pristine MoS_2–NiS_2 (3.2×10^{-4} mol mg^{-1}). Overall, increased surface area and more catalytically active sites positively contribute toward the enhanced catalytic activity of MoS_2–NiS_2/G. Moreover, the HER activity of the resulting MoS_2–NiS_2/G was also assessed under alkaline conditions (1.0 M KOH). The LSV curves displayed in Fig. 3e represent the smallest onset potential for MoS_2–NiS_2/G (72 mV), which is significantly lower than pristine MoS_2/NiS_2 (130 mV), NiS_2 (183 mV) and MoS_2 (272 mV). Similarly, for MoS_2–NiS_2/G only overpotential of 141 mV was required to attain the current density of 10 mA cm^{-2} (η_{10}), which is considerably lower compared to the MoS_2/NiS_2 (η_{10} = 205 mV), NiS_2 (η_{10} = 245 mV) and MoS_2 (η_{10} = 335 mV). Moreover, the HER performance of MoS_2–NiS_2/G in an alkaline medium stands superior when compared to other recently reported electrocatalyst systems based on transition metal–sulphides (Table S2, ESI†). Likewise, the Tafel slopes derived from the corresponding Tafel plots (Fig. 3f) indicate a smaller value for MoS_2–NiS_2/G (77 mV dec^{-1}) in comparison to the MoS_2–NiS_2 (116 mV dec^{-1}), NiS_2 (158 mV dec^{-1}), and MoS_2 (227 mV dec^{-1}), respectively, revealing the superior HER kinetics for MoS_2–NiS_2/G. The Nyquist plots in (Fig. S12a, ESI†)

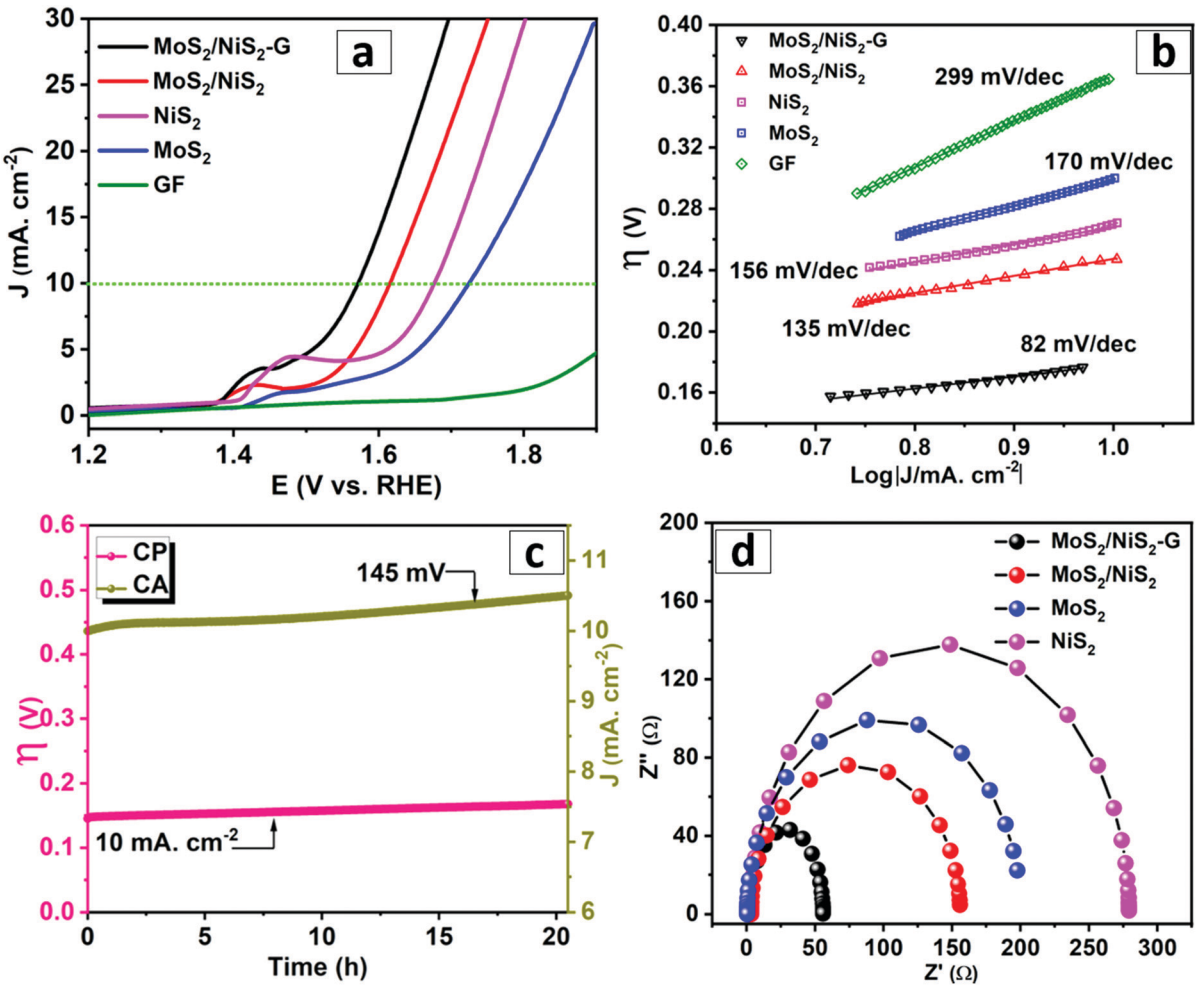

Fig. 4 (a) Polarization curves and (b) the corresponding Tafel plots of the resulting samples for the OER. (c) Chronopotentiometric and chronoamperometric curve of the OER for MoS_2–NiS_2/G and (d) EIS curves for the resulting samples.

provided further evidence of better conductivity of MoS_2–NiS_2/G in comparison to the MoS_2–NiS_2 under an alkaline medium, primarily owing to the presence of graphene. Similarly, the electrochemical stability of MoS_2–NiS_2/G was estimated by continuous CV tests in the alkaline electrolyte, showing the marginal change in current density after 3000 cycles (Fig. S12b, ESI†). The steady time-dependent current density curve further underlines the stable catalytic activity of NiS_2/MoS_2–G (inset Fig. S12b, ESI†). Overall, owing to its remarkable electrocatalytic activity, the NiS_2/MoS_2–G nanohybrid is a cheaper substitute for HER catalysts used for large-scale practical water-splitting applications in both acidic and alkaline media.

Oxygen evolution reaction (OER) study

In addition to the excellent HER activity in both acidic and alkaline electrolytes, the catalytic performance of MoS_2–NiS_2/G was further assessed for OER studies. The evaluation of the electrocatalytic activity of the as-obtained nanohybrids toward the OER was performed in 1 M KOH (Fig. 4). The LSV curve of the MoS_2–NiS_2/G and MoS_2–NiS_2 nanohybrids reveals two primary features, a sharp signal associated with the oxidation of Ni^{2+} located at around 1.43 V[60] and an oxidation current that rises quickly at potentials greater than 1.46 V along with the appearance of bubbles on the electrode, which designates that the OER is proceeding. The LSV of MoS_2–NiS_2/G displays a small overpotential of 320 mV@10 mA cm^{-2} (η_{10}). Strikingly, the recorded overpotential for MoS_2–NiS_2/G was much higher compared to the MoS_2–NiS_2 hybrid (370 mV). This increment was ascribed to the synergistic effects brought by MoS_2–NiS_2 with defect-rich exposed active sites supported on graphene conductive support. Moreover, these results underline the remarkable OER performance of MoS_2–NiS_2/G nanohybrids over other reported non-noble metal electrocatalysts (Table S3, ESI†). The calculated Tafel slope (Fig. 4b) for MoS_2–NiS_2/G (82 mV dec^{-1}) was considerably lower than that of pristine MoS_2–NiS_2 and in close proximity to that of RuO_2 (65.5 mV dec^{-1}).[61] Overall, the results reaffirm the better kinetics and the enhanced electrocatalytic activity of MoS_2–NiS_2/G for OER. Furthermore, the OER stability of the MoS_2–NiS_2/G electrode was tested applying simultaneous chronopotnetiometry (CP), and chronoamperometry (CA) tests over the span of 20 h (Fig. 4c). These tests show no obvious change in initial applied current density and potential, respectively, signifying consistent conductivity, durability, and mass transport in the OER study. Similarly, the fitted EIS data (Fig. 4d)

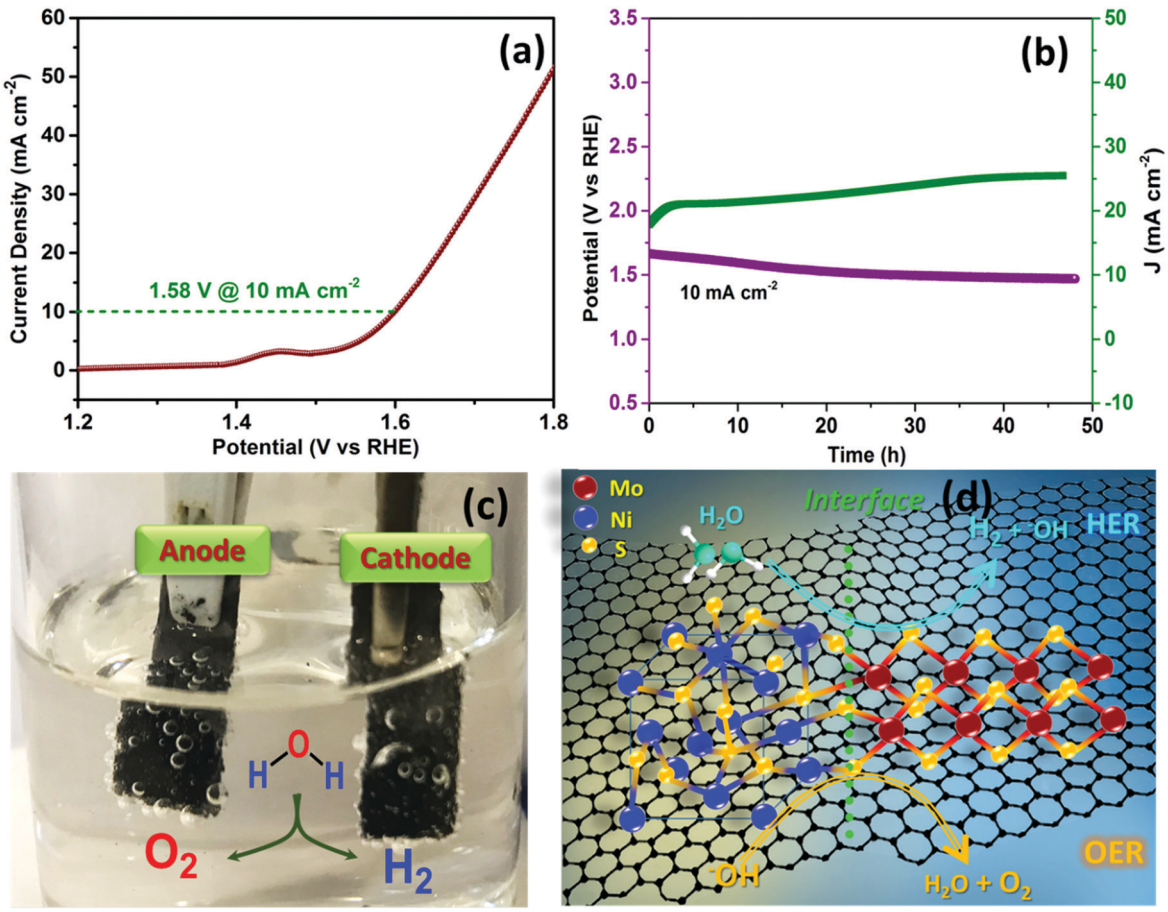

Fig. 5 (a) LSV curves of the MoS_2–NiS_2/G||MoS_2–NiS_2/G two-electrode system used as both the cathode and anode in 1 M KOH, (b) chrono-potentiometry and chrono-amperometry curves at a constant current density of 10 mA cm^{-2} and potential for overall water splitting, (c) optical photograph showing the generation of hydrogen and oxygen bubbles from overall water splitting on MoS_2–NiS_2/G as both the anode and cathode and, (d) schematic representation of the overall water splitting using MoS_2–NiS_2/G as a bifunctional electrocatalyst for simultaneous HER and OER.

obtained at set-potentials of 1.5 V revealed Nyquist plots that exhibit considerably reduced semicircles corresponding to MoS_2–NiS_2/G compared to pristine MoS_2–NiS_2 indicating lower resistance. The higher conductivity of the MoS_2–NiS_2/G catalyst was attributed to the graphene conductive framework, which facilitates the effective electrical charge transfer thereby minimizing the possible parasitic Ohmic losses.

Overall water splitting

Motivated by the superior OER and HER activities, we further demonstrated the feasibility of using MoS_2–NiS_2/G as a bifunctional electrocatalyst for efficient overall water splitting (Fig. 5a). The MoS_2–NiS_2/G nanohybrid was assembled as both anode and cathode in a two-electrode configuration and tested under alkaline conditions. It was noted that the potential of only 1.58 V is required to reach a current density of 10 mA cm^{-2} whereas MoS_2–NiS_2 hybrids require a potential of 1.84 V at J = 10 mA cm^{-2}. The measured potential is highly competitive with the benchmark noble catalysts such as IrO_2–Pt (1.7 V)[31] as well as the previously reported Mo–Ni sulphide based bifunctional electrocatalysts measured at J = 10 mA cm^{-2} in an alkaline medium, for example, NiS–MoS_2/G (MoS_2–NiS_2–NF (1.64 V),[38] MoS_2–NiS_2 (1.59 V),[33] MoS_2–NiS (1.60 V),[62] MoS_2–NiS (1.64 V),[63] NiS–NiS_2 (1.62 V),[64] NiS–Ni_2P (1.67 V)[65] and Co_3O_4@MoS_2 (1.59 V).[44] Moreover, the CA and CP studies confirmed the excellent long term stability of the resulting electrocatalysts during overall water splitting in alkaline media (Fig. 5b). The CA test performed at 1.60 V over a period of 2 days shows an initial current increase and attains constant current density. Similarly, vigorous H_2 and O_2 gas evolution was observed at the respective cathode and anode electrodes (Fig. 5c). The MoS_2–NiS_2/G catalyst demonstrates superior overall water splitting performance compared to the state-of-the-art electrocatalysts. Such high electrocatalytic performance of MoS_2–NiS_2/G was attributed due to the *in situ* grown heterogeneous MoS_2/NiS_2 nanostructure loaded with defect-rich synergistic interfaces supported on a conductive graphene framework (Fig. 5d) that warrants abundant active sites and high-rate and long-life stability.

Conclusions

In summary, we have developed a facile and technologically scalable approach for the preparation of a noble-metal free Mo–Ni based robust bifunctional electrocatalyst. A solid-state *in situ* growth strategy manifests the formation of nanostructured interface engineered MoS_2–NiS_2 distributed within the graphene surface. The synergistic contribution leads to increased catalytically active sites, enlarged surface area, and electrical conductivity in the resulting MoS_2/NiS_2–G nanohybrid. The catalyst exhibits exceptional HER catalytic activity with lower overpotentials and smaller Tafel slopes in both acidic (152 mV @10 mA cm^{-2}/53 mV dec^{-1}) and alkaline (141 mV@10 mA cm^{-2}/77 mV dec^{-1}) electrolytes, respectively. The resulting electrocatalysts also showed excellent OER efficiency. Moreover, the MoS_2/NiS_2–G only required an overpotential of 1.58 V to achieve overall water splitting at a current density of 10 mA cm^{-2} and displays consistent catalytic activity for about 48 h. Given the low cost and environmental benignity, the present work offers a valuable method for rational design and interface engineering of low-cost earth-abundant metal-based efficient bifunctional electrocatalysts for large scale sustainable energy production and other environmental applications.

Conflicts of interest

There are no conflicts to declare.

Acknowledgements

This work was supported by the Abu Dhabi Department of Education and Knowledge (ADEK) Award for Research Excellence (AARE17). The authors also thank Dr Shashikant Patole (KU-Physics Department) for HRTEM images, and Dr Vishwanath Kalyani, IIT-Mumbai for XPS analysis.

Notes and references

1 M. S. Dresselhaus and I. L. Thomas, *Nature*, 2001, **414**, 332–337.
2 C. Sweeney, R. J. Bessa, J. Browell and P. Pinson, *Wires Energy Environ.*, 2019, **365**, e365, DOI: 10.1002/wene.365.
3 M. Zeng and Y. Li, *J. Mater. Chem. A*, 2015, **3**, 14942–14962.
4 Y. Zhang, M. Xie, V. Adamaki, H. Khanbareh and C. R. Bowen, *Chem. Soc. Rev.*, 2017, **46**, 7757–7786.
5 B. You and Y. Sun, *Acc. Chem. Res.*, 2018, **51**, 1571–1580.
6 Q. Shi, C. Zhu, D. Du and Y. Lin, *Chem. Soc. Rev.*, 2019, **48**, 3181–3192.
7 M. Zhang, J. Chen, H. Li, P. Cai, Y. Li and Z. Wen, *Nano Energy*, 2019, **61**, 576–583.
8 C. Xie, D. Yan, W. Chen, Y. Zou, R. Chen, S. Zang, Y. Wang, X. Yao and S. Wang, *Mater. Today*, 2019, **31**, 47–68.
9 M. Shao, Q. Chang, J.-P. Dodelet and R. Chenitz, *Chem. Rev.*, 2016, **116**, 3594–3657.
10 Q. Wang, Z. L. Zhao, S. Dong, D. He, M. J. Lawrence, S. Han, C. Cai, S. Xiang, P. Rodriguez, B. Xiang, Z. Wang, Y. Liang and M. Gu, *Nano Energy*, 2018, **53**, 458–467.
11 X. Chia and M. Pumera, *Chem. Soc. Rev.*, 2018, **47**, 5602–5613.
12 H. Xu, S. Ci, Y. Ding, G. Wang and Z. Wen, *J. Mater. Chem. A*, 2019, **7**, 8006–8029.
13 P. Cai, Y. Li, G. Wang and Z. Wen, *Angew. Chem., Int. Ed.*, 2018, **57**, 3910–3915.
14 G. Fu and J.-M. Lee, *J. Mater. Chem. A*, 2019, **7**, 9386–9405.
15 Y. Guo, T. Park, J. W. Yi, J. Henzie, J. Kim, Z. Wang, B. Jiang, Y. Bando, Y. Sugahara, J. Tang and Y. Yamauchi, *Adv. Mater.*, 2019, **31**, 1807134.
16 L. Zhao, Z. Yang, Q. Cao, L. Yang, X. Zhang, J. Jia, Y. Sang, H.-J. Wu, W. Zhou and H. Liu, *Nano Energy*, 2019, **56**, 563–570.

17 Z. Chen, X. Duan, W. Wei, S. Wang and B.-J. Ni, *J. Mater. Chem. A*, 2019, **7**, 14971–15005.
18 S. P. Lonkar, V. V. Pillai and S. M. Alhassan, *Int. J. Hydrogen Energy*, 2020, **45**, 10475–10485.
19 Z. Zhang, X. Lv, Y. Chen, P. Zhang, M. Sui, H. Liu and X. Sun, *Nanomaterials*, 2019, **9**, 292.
20 D. Zhang, H. Mou, L. Chen, D. Wang and C. Song, *Appl. Surf. Sci.*, 2020, **510**, 145483.
21 M. Fang, G. F. Dong, R. J. Wei and J. C. Ho, *Adv. Energy Mater.*, 2017, 7.
22 Z. J. Chen, X. G. Duan, W. Wei, S. B. Wang and B. J. Ni, *J. Mater. Chem. A*, 2019, **7**, 14971–15005.
23 U. Gupta and C. N. R. Rao, *Nano Energy*, 2017, **41**, 49–65.
24 T. F. Jaramillo, K. P. Jørgensen, J. Bonde, J. H. Nielsen, S. Horch and I. Chorkendorff, *Science*, 2007, **317**, 100–102.
25 C. Tang, Z. H. Pu, Q. Liu, A. M. Asiri, Y. L. Luo and X. P. Sun, *Int. J. Hydrogen Energy*, 2015, **40**, 4727–4732.
26 J. T. Ren and Z. Y. Yuan, *ACS Sustainable Chem. Eng.*, 2017, **5**, 7203–7210.
27 J. Wang, X. Yue, Y. Yang, S. Sirisomboonchai, P. Wang, X. Ma, A. Abudula and G. Guan, *J. Alloys Compd.*, 2020, **819**, 153346.
28 B.-W. Zhang, H.-L. Yang, Y.-X. Wang, S.-X. Dou and H.-K. Liu, *Adv. Energy Mater.*, 2018, **8**, 1703597.
29 M. Escudero-Escribano, K. D. Jensen and A. W. Jensen, *Curr. Opin. Electrochem.*, 2018, **8**, 135–146.
30 S. D. Guan, X. L. Fu, Z. Z. Lao, C. H. Jin and Z. J. Peng, *Sustainable Energy Fuels*, 2019, **3**, 2056–2066.
31 J. Zhang, T. Wang, D. Pohl, B. Rellinghaus, R. Dong, S. Liu, X. Zhuang and X. Feng, *Angew. Chem., Int. Ed.*, 2016, **55**, 6702–6707.
32 Y. Q. Yang, K. Zhang, H. L. Ling, X. Li, H. C. Chan, L. C. Yang and Q. S. Gao, *ACS Catal.*, 2017, **7**, 2357–2366.
33 J. H. Lin, P. C. Wang, H. H. Wang, C. Li, X. Q. Si, J. L. Qi, J. Cao, Z. X. Zhong, W. D. Fei and J. C. Feng, *Adv. Sci.*, 2019, 6.
34 Z. B. Chen, D. Cummins, B. N. Reinecke, E. Clark, M. K. Sunkara and T. F. Jaramillo, *Nano Lett.*, 2011, **11**, 4168–4175.
35 B. Hasa, E. Martino, J. Vakros, G. Trakakis, C. Galiotis and A. Katsaounis, *ChemElectroChem*, 2019, **6**, 4970–4979.
36 Q. Hu, G. Li, Z. Han, Z. Wang, X. Huang, H. Yang, Q. Zhang, J. Liu and C. He, *J. Mater. Chem. A*, 2019, **7**, 14380–14390.
37 J. Lin, P. Wang, H. Wang, C. Li, X. Si, J. Qi, J. Cao, Z. Zhong, W. Fei and J. Feng, *Adv. Sci.*, 2019, **6**, 1900246.
38 P. Kuang, M. He, H. Zou, J. Yu and K. Fan, *Appl. Catal., B*, 2019, **254**, 15–25.
39 S. Li, T. Chen, J. Wen, P. Gui and G. Fang, *Nanotechnology*, 2017, **28**, 445407.
40 M. A. Bissett, I. A. Kinloch and R. A. W. Dryfe, *ACS Appl. Mater. Interfaces*, 2015, **7**, 17388–17398.
41 Y. Zhang, F. Lu, L. Pan, Y. Xu, Y. Yang, Y. Bando, D. Golberg, J. Yao and X. Wang, *J. Mater. Chem. A*, 2018, **6**, 11978–11984.
42 S.-L. Yang, H.-B. Yao, M.-R. Gao and S.-H. Yu, *CrystEngComm*, 2009, **11**, 1383–1390.
43 S. P. Lonkar, V. Pillai, A. Abdala and V. Mittal, *RSC Adv.*, 2016, **6**, 81142–81150.
44 J. Liu, J. Wang, B. Zhang, Y. Ruan, H. Wan, X. Ji, K. Xu, D. Zha, L. Miao and J. Jiang, *J. Mater. Chem. A*, 2018, **6**, 2067–2072.
45 J. Hu, C. X. Zhang, L. Jiang, H. Lin, Y. M. An, D. Zhou, M. K. H. Leung and S. H. Yang, *Joule*, 2017, **1**, 383–393.
46 S. P. Lonkar, V. V. Pillai and S. M. Alhassan, *ACS Appl. Nano Mater.*, 2018, **1**, 3114–3123.
47 T. An, Y. Wang, J. Tang, W. Wei, X. Cui, A. M. Alenizi, L. Zhang and G. Zheng, *J. Mater. Chem. A*, 2016, **4**, 13439–13443.
48 A. R. Gerson and T. Bredow, *Surf. Interface Anal.*, 2000, **29**, 145–150.
49 Y. P. Zhu, C. Guo, Y. Zheng and S.-Z. Qiao, *Acc. Chem. Res.*, 2017, **50**, 915–923.
50 H. Li, Q. Zhang, C. C. R. Yap, B. K. Tay, T. H. T. Edwin, A. Olivier and D. Baillargeat, *Adv. Funct. Mater.*, 2012, **22**, 1385–1390.
51 T. Suzuki, K. Uchinokura, T. Sekine and E. Matsuura, *Solid State Commun.*, 1977, **23**, 847–852.
52 C. Ouyang, X. Wang and S. Wang, *Chem. Commun.*, 2015, **51**, 14160–14163.
53 J.-B. Wu, M.-L. Lin, X. Cong, H.-N. Liu and P.-H. Tan, *Chem. Soc. Rev.*, 2018, **47**, 1822–1873.
54 S. Dou, X. Wang and S. Wang, *Small Methods*, 2019, **3**, 1800211.
55 J. Benson, M. Li, S. Wang, P. Wang and P. Papakonstantinou, *ACS Appl. Mater. Interfaces*, 2015, **7**, 14113–14122.
56 M. R. G. de Chialvo and A. C. Chialvo, *J. Electroanal. Chem.*, 1994, **372**, 209–223.
57 P. Yu, L. Wang, Y. Xie, C. Tian, F. Sun, J. Ma, M. Tong, W. Zhou, J. Li and H. Fu, *Small*, 2018, **14**, 1801717.
58 X. Liu, L. Liu, Y. Wu, Y. Wang, J. Yang and Z. Wang, *RSC Adv.*, 2019, **9**, 13820–13828.
59 A. P. Murthy, J. Theerthagiri, J. Madhavan and K. Murugan, *Phys. Chem. Chem. Phys.*, 2017, **19**, 1988–1998.
60 M. W. Louie and A. T. Bell, *J. Am. Chem. Soc.*, 2013, **135**, 12329–12337.
61 R. R. Rao, M. J. Kolb, N. B. Halck, A. F. Pedersen, A. Mehta, H. You, K. A. Stoerzinger, Z. Feng, H. A. Hansen, H. Zhou, L. Giordano, J. Rossmeisl, T. Vegge, I. Chorkendorff, I. E. L. Stephens and Y. Shao-Horn, *Energy Environ. Sci.*, 2017, **10**, 2626–2637.
62 Z. Zhai, C. Li, L. Zhang, H.-C. Wu, L. Zhang, N. Tang, W. Wang and J. Gong, *J. Mater. Chem. A*, 2018, **6**, 9833–9838.
63 Q. Qin, L. Chen, T. Wei and X. Liu, *Small*, 2019, **15**, 1803639.
64 Q. Li, D. Wang, C. Han, X. Ma, Q. Lu, Z. Xing and X. Yang, *J. Mater. Chem. A*, 2018, **6**, 8233–8237.
65 X. Xiao, D. Huang, Y. Fu, M. Wen, X. Jiang, X. Lv, M. Li, L. Gao, S. Liu, M. Wang, C. Zhao and Y. Shen, *ACS Appl. Mater. Interfaces*, 2018, **10**, 4689–4696.